NDT&E International 112 (2020) 102239

Contents lists available at ScienceDirect

NDT and E International

journal homepage: http://www.elsevier.com/locate/ndteint

Photothermal image reconstruction in opaque media with virtual wave backpropagation

G. Thummerer [a,*], G. Mayr [a], P.D. Hirsch [b], M. Ziegler [b], P. Burgholzer [c]

[a] Josef Ressel Centre for Thermal NDE of Composites, University of Applied Sciences Upper Austria, 4600, Wels, Austria
[b] Bundesanstalt für Materialforschung und -prüfung (BAM), 12200, Berlin, Germany
[c] RECENDT - Research Centre for Nondestructive Testing, 4040, Linz, Austria

ARTICLE INFO

Keywords:
Thermography
Photothermal Technique
Virtual wave concept
Image reconstruction

ABSTRACT

Thermographic reconstruction of defects that lie in the bulk of a sample is a difficult task because entropy production during heat diffusion leads to information loss. To reconstruct defects one has to solve an inverse heat conduction problem. The quality of the reconstruction is closely related to the information content of the observed data set that is reflected by the decreasing ability to spatially resolve a defect with growing defect depth. In this work we show a 2D reconstruction of rectangular slots with different width-to-depth ratios in a metallic sample. For this purpose, we apply the virtual wave concept and incorporate positivity and sparsity as prior information to overcome the diffusion-based information loss partially. The reconstruction is based on simulated and experimental pulse thermography data. In the first reconstruction step, we compute a virtual wave field from the surface temperature data. This allows us, in the second step, to use ultrasonic backpropagation methods for image reconstruction.

1. Introduction

In recent decades the number of industrial applications of the non-destructive testing method active thermography has significantly grown [1,2]. For active thermography the specimen is stimulated, e.g. by a flash lamp, laser or induction of eddy current, to obtain a temperature rise compared to the initial state. This change in temperature or more precisely the change in electromagnetic radiation in the infrared regime, is then detected on the surface of the specimen using an infrared (IR)-camera. Since defects like, e.g. cracks, have different physical properties compared to the bulk material of the specimen they can be detected. The advantages of active thermography are that large components can be quickly tested due to the focal plane array of the IR-camera. The specimen can also be inspected contactless, and the resulting images are readily assessable by non-experts.

The detected surface temperature fulfils the diffusion equation. Here, the disadvantage of thermography becomes visible. The heat diffusion equation describes an irreversible process that is characterized by entropy production, that is directly connected to information loss [3]. This loss of information is responsible for the thermal detection limit. For a spatially homogeneous and temporally *Dirac-delta*-like heating of a specimen there exists a basic rule for the thermal detection limit that states: The defect diameter-to-depth ratio must be greater than 2 [1,4]. Otherwise, the defect cannot be detected reliably.

In state-of-the-art thermal NDE methods, a one-dimensional (1D) thermal model is used for depth estimation and in some cases for the characterization of the thermal resistance between the bulk material and the defect [5,6]. These 1D approaches become inaccurate for defect visualization when the inspected objects have a complex shape or the defects have a finite or irregular boundary, taking into account that the anisotropic heat conduction of composites amplifies these effects [7]. To overcome these problems, Kaiplavil and Mandelis [8] reported a depth-resolved photothermal imaging modality, the so-called truncated-correlation photothermal coherence tomography (TC-PCT), which enables a 3D visualization through the deconvolution of thermal responses from axially discrete sources. This improves the depth resolution to overcome image blurring limitations [9]. Another approach for more accuracy regarding the effects of lateral heat diffusion is the solution of the multi-dimensional heat conduction equation for a model-based image reconstruction [10]. Several studies use the finite-element method for the numerical solution of the heat conduction problems to realize the defect reconstruction [11–13]. Thermographic image reconstruction based on analytical solutions of the temperature field is applied for buried heat sources [14] and also for defects in

* Corresponding author.
E-mail address: gregor.thummerer@fh-wels.at (G. Thummerer).

https://doi.org/10.1016/j.ndteint.2020.102239
Received 30 October 2019; Received in revised form 7 February 2020; Accepted 17 February 2020
Available online 22 February 2020

composite materials [15]. The multi-dimensional thermal wave field modelling always results in large-scale reconstruction problems, which are computationally intensive and severely ill-posed. To partly compensate for the information loss and to improve the quality of the multidimensional reconstruction, Burgholzer et al. introduced a new approach for thermographic imaging, the so-called virtual wave concept (VWC) [16]. The idea of VWC is to transform the surface temperature detected by an IR-camera into a virtual wave field. The first applications of a transformation of the diffusive electromagnetic wave into a wave field was shown by Lee et al. [17,18] and Gershenson [19] for geophysical applications. While the surface temperature fulfils the diffusion equation, the virtual wave field obeys the wave equation. In contrast to the diffusion equation, the wave equation describes a reversible process. Due to this fact, reconstruction methods well known from ultrasonic testing can be employed for 3D thermographic imaging. Thus, in principle VWC is a two-step inverse process. The first inverse problem is severely ill-posed due to information loss that is equal to the entropy production during heat diffusion.

To enhance the quality of the inverse solution one can introduce prior information, such as positivity and sparsity [20,21]. In contrast to the 1D virtual wave field, the 2D acoustic virtual wave exhibits negative data points with respect to time, hence the additional information positivity is not direct applicable. For one IR-camera pixel the information gain incorporating positivity is only a factor of two, but if we consider the n-pixel of the camera we have an information gain of 2^n. In order to apply positivity, these data sets have to be transformed. For 3D this is readily done by spherical projections that correspond to a time integral of the 3D virtual wave. In 2D, the *Abel* transformation or circular projection has to be applied in order to increase the information content for the regularization process [22,23]. Note, in the discrete case positivity is introduced by a simple matrix multiplication using the Abel-trafo matrix which has full rank. Hence, the inverse of the Abel-trafo matrix exists. Moreover, the prior information sparsity is introduced, because usually we have only a few defects in practise related specimens, e.g. delaminations or cracks. Consequently, we have only a few point scatterers which leads to a sparse virtual wave field. Sparsity is introduced by an appropriate formulation of the objective function using L_1 norm minimization.

In this work we show 2D reconstructions of rectangular slots in a metallic sample with different defect width-to-depth ratios. An overview of the process steps using VWC for a 2D reconstruction problem is illustrated in Fig. 1. In the first section we give an overview of the regularization and reconstruction tools used. We show how additional information can be incorporated into the regularization process. Moreover, we discuss the link between the virtual wave field and its projection on positive data points. Heat conduction simulations with the Finite Element Method (FEM) and experimental investigations based on pulsed thermography measurements are used to validate the modified virtual wave concept.

2. Virtual wave concept

Referring to the virtual wave concept (VWC), one can compute the multidimensional temperature distribution $T(\mathbf{r},t)$ based on so-called virtual waves $T_{\text{virt}}(\mathbf{r},t')$ for the same position vector $\mathbf{r}$ but different time scales t and t', respectively. According to Ref. [16], the formal relationship is given by a Fredholm integral of the first kind:

$$T(\mathbf{r},t) = \int_{-\infty}^{\infty} K(t,t')T_{\text{virt}}(\mathbf{r},t')\,\mathrm{d}t' \qquad (1)$$

$$\text{with } K(t,t') = \frac{c}{\sqrt{\pi\alpha t}}\exp\left(-\frac{c^2t'^2}{4\alpha t}\right) \text{ for } t>0.$$

$K(t,t')$ is the transformation kernel between temperature and virtual waves. It contains the characteristic parameters thermal diffusivity α and virtual speed of sound c, which describes the speed of heat and virtual wave propagation.

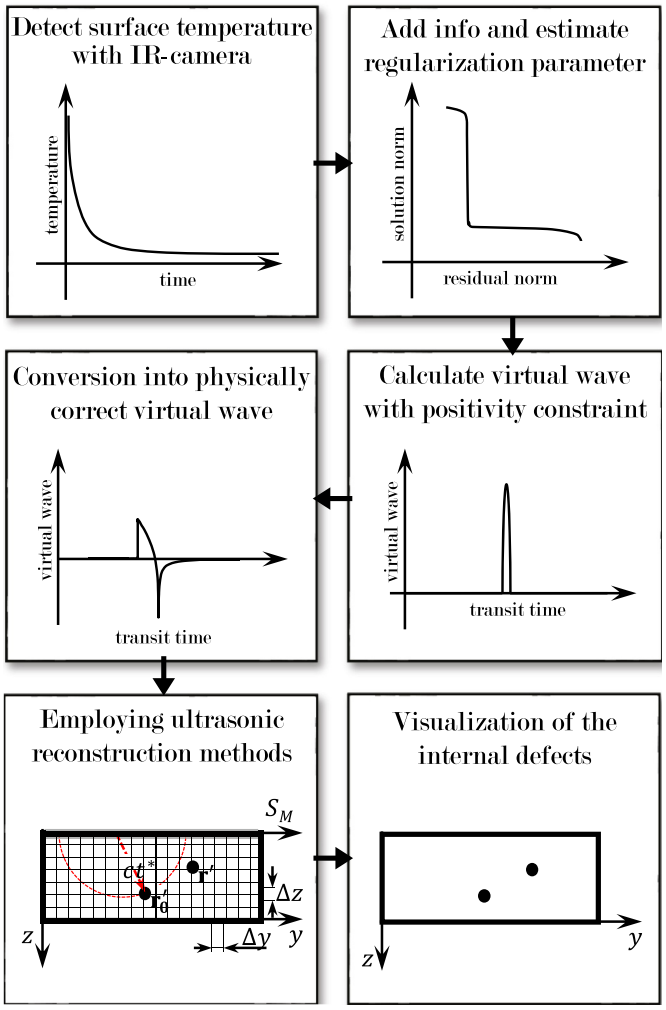

Fig. 1. Overview of the process steps using VWC for a 2D problem incorporating additional information.

2.1. Incorporating positivity as prior information

Thermal diffusion causes entropy production and hence information loss. In contrast to the 1D virtual wave field [24], the 2D and 3D virtual wave fields contains negative data points. To increase the information content in the regularization process, the data set is projected via spherical or circular means onto positive data points.

In this work we consider 2D photothermal temperature data of an opaque material with embedded slots. Thermal waves are introduced at the sample surface. Simultaneously, the data is recorded on the observation plane that correspond to the sample surface. The thermal waves propagate through the solid until their flow is perturbed by the slots. Consequently, secondary thermal wave sources are introduced at the boundaries of the slots [25]. Due to the fact that the superposition principle is valid for both heat and wave equation, we can imagine the secondary thermal wave sources as accumulation of point scatterers that introduce heat in the semi infinite body. According to VWC we transform these point scatterers into an "acoustic" virtual wave. Consequently, the secondary thermal waves sources exhibit the bimodal characteristic of a 2D photoacoustic wave form (see Fig. 1 middle-left box) [26]. As one can see the 2D photoacoustic wave exhibits negative data points. In this section, we show how the bimodal virtual waves can

be projected onto a positive data set in order to incorporate positivity in the regularization process. We consider a 2D data set. The corresponding virtual wave field $T_{\text{virt}}(x,y,t)$ is described by the 2D photoacoustic wave equation:

$$\left[\Delta_{2D} - \frac{1}{c^2}\frac{\partial^2}{\partial t'^2}\right] T_{\text{virt}}(x,y,t') = -\frac{1}{c^2}\frac{\partial}{\partial t'} T_0(x,y)\delta(t'), \tag{2}$$

where $T_0(x,y)$ is an initial temperature distribution. The solution of the wave equation is given by Ref. [27]:

$$T_{\text{virt}}(x,y,t') = \frac{\partial}{\partial t'}\left[\frac{1}{2\pi c}\iint\limits_{\sqrt{(x-x')^2+(y-y')^2}<ct'} \frac{T_0(x',y')\,\mathrm{d}x'\mathrm{d}y'}{\sqrt{c^2t'^2-(x-x')^2-(y-y')^2}}\right]. \tag{3}$$

Now let us consider a finite number of $n = 1, 2, \ldots, N$ detection points (x^n, y^n) which are positioned on a closed or open detector curve outside the specimen. According to Ref. [28] we can write:

$$T_{\text{virt}}(x^n,y^n,t') = \frac{\partial}{\partial t'}\left[\frac{1}{c}\int_0^{ct'} \frac{r(M_nT_0)(x^n,y^n,r)\,\mathrm{d}r}{\sqrt{c^2t'^2-r^2}}\right]$$
$$\text{with} \tag{4}$$
$$(M_nT_0)(x^n,y^n,r) = \frac{1}{2\pi r}\oint\limits_{\sqrt{(x^n-x')^2+(y^n-y')^2}=r} T_0(x',y')\,\mathrm{d}C',$$

where $(M_nT_0)(x^n,y^n,r)$ are the circular means of T_0 at detection point (x^n,y^n) with radius r. Eq. (4) is of Abel-type and can be written as

$$T_{\text{virt}}(x^n,y^n,t') = \frac{\partial}{\partial t'}\frac{1}{c}\mathscr{A}\{(M_nT_0)(x^n,y^n,r)\}$$
$$\text{with}\quad \mathscr{A}\{(M_nT_0)(x^n,y^n,r)\} = \int_0^{ct'}\frac{r(M_nT_0)(x^n,y^n,r)}{\sqrt{c^2t'^2-r^2}}\mathrm{d}r \tag{5}$$

Herein, $\mathscr{A}\{\cdot\}$ is the Abel transformation operator. Based on the inverse Abel transformation the circular means $(M_nT_0)(x^n,y^n,r)$ can be calculated explicitly [22,28]:

$$(M_nT_0)(x^n,y^n,r) = \frac{2c}{\pi}\int_0^{r/c}\frac{T_{\text{virt}}(x^n,y^n,t')}{\sqrt{r^2-c^2t'^2}}\mathrm{d}t'. \tag{6}$$

Due to Eq. (5) we can see that the projection onto positive data points (the circular means) and the virtual wave field, which fulfils the 2D wave equation, are connected by the Abel transformation. The Abel transformation relates the computed virtual wave signals, that are a function of time, to its circular projection and consequently to the circular integrals of a photothermal source with radius r and center point (x^n,y^n).

2.2. Discrete data

Let us consider the *Fredholm* integral of the first kind, shown Eq. (2). Due to the fact that thermography data is discrete in time and space, Eq. (2) is first discretized:

$$\mathbf{T} = \mathbf{K}\mathbf{T}_{\text{virt}}. \tag{7}$$

The aim is to calculate $\mathbf{T}_{\text{virt}}$ based on the measured temperature field $\mathbf{T}$. This is a severely ill-posed inverse problem. To incorporate additional information the inverse problem must be reformulated. Therefore, we compute the circular projections of the virtual wave $\mathbf{T}_{\text{virt}}$ with respect to Eq. (5) with the inverse *Abel*-trafo matrix $\mathbf{A}^{-1}$ in the following manner [22]:

$$\mathbf{M}_{\text{virt}} = \mathbf{A}^{-1}\mathbf{T}_{\text{virt}}. \tag{8}$$

Consequently, we can substitute $\mathbf{T}_{\text{virt}}$ by $\mathbf{A}\mathbf{M}_{\text{virt}}$ in Eq. (7). This yields the new inverse problem

$$\mathbf{T} = \mathbf{K}\mathbf{A}\mathbf{M}_{\text{virt}} = \overline{\mathbf{K}}\mathbf{M}_{\text{virt}}$$
$$\text{with}\quad \overline{\mathbf{K}} = \mathbf{K}\mathbf{A}. \tag{9}$$

Note, the discrete Abel-trafo matrix already respects the time derivative $\frac{\partial}{\partial t'}$ in Eq. (5).

2.3. Solve the inverse problem

Computing the circular projection $\mathbf{M}_{\text{virt}}$ with positivity constraint based on the linear matrix equation Eq. (9) is a severely ill posed inverse problem. Therefore, we need some kind of regularization to get an appropriate solution for $\mathbf{M}_{\text{virt}}$. Basically, one can distinguish direct and iterative regularization methods. Here we use the alternating direction method of multipliers (ADMM) [29,30], that is an iterative regularization scheme to incorporate the additional information sparsity. The intention of ADMM is to split the objective function and to introduce a constraint. The following objective function is minimized [21].

$$\frac{1}{2}\left|\left|\overline{\mathbf{K}}\mathbf{M}_{\text{virt}} - \mathbf{T}\right|\right|_2^2 + \lambda\left|\left|\mathbf{M}_{\text{virt}}\right|\right|_1$$
$$\text{subject to}\quad \mathbf{M}_{\text{virt}} - \mathbf{z} = 0 \tag{10}$$

In Eq. (10) the 2-norm represents the residual norm and the 1-norm represents the solution norm. The 1-norm incorporates sparsity, so we assume that the solution matrix is sparse. λ is a regularization parameter, that can be determined e.g. by the *L-curve*-method [31]. To get an iterative procedure we form the *Lagrangian* using the objective function and the constraint. The optimization of the dependent variables yields the subsequent iteration steps [21]:

$$\mathbf{M}_{\text{virt}}^{k+1} := (\overline{\mathbf{K}}^{\mathrm{T}}\overline{\mathbf{K}} + \rho\mathbf{I})^{-1}\left[\overline{\mathbf{K}}^{\mathrm{T}}\mathbf{T} + \rho\left(\mathbf{z}^k - \mathbf{u}^k\right)\right]$$
$$\mathbf{z}^{k+1} := S_{\lambda/\rho}\left(\mathbf{M}_{\text{virt}}^{k+1} + \mathbf{u}^k\right) \tag{11}$$
$$\mathbf{u}^{k+1} := \mathbf{u}^k + \mathbf{M}_{\text{virt}}^{k+1} - \mathbf{z}^{k+1}.$$

In Eq. (11) ρ is a penalty parameter, that makes the algorithm faster and more robust. $S_{\lambda/\rho}$ is a soft-threshold operator. The thresholding is applied only onto positive entries. Negative entries are set to zero, hence positivity is enforced. The $\mathbf{u}$ vector contains the *Lagrangian* multipliers.

2.4. Image reconstruction

The use of image reconstruction techniques is intended to simplify the interpretation of the measurement result and to increase the signal-to-noise (SNR) ratio. This makes inner structures visible, which cannot be found in the classic B-scan image. To improve the sensitivity and resolution of the virtual wave field, we use the synthetic aperture focusing technique (SAFT) [32,33]. The principle of time domain (T)-SAFT is depicted in Fig. 2.

Thermography allows the simultaneous acquisition of a large number of signals (up to 10^6) over the surface of a test specimen, which is equivalent to a large aperture. In the case of optically excited pulsed thermography the generation and detection of the virtual waves are focused on the same location on the surface ($z = 0$). The virtual wave field originates from every point of the surface simultaneously as a plane wave. A diffraction source, e.g. the tip of a defect, is located at a position $\mathbf{r}'$ inside the specimen (Fig. 2). This disturbance re-radiates the virtual wave field originating from the specimen surface with a time delay. The theoretical scattering hyperbola can be calculated for each voxel with the coordinates (x',y',z') if the speed of sound c is known. Along this curve, an integration of the scalar measurement data T_{virt} is then carried out:

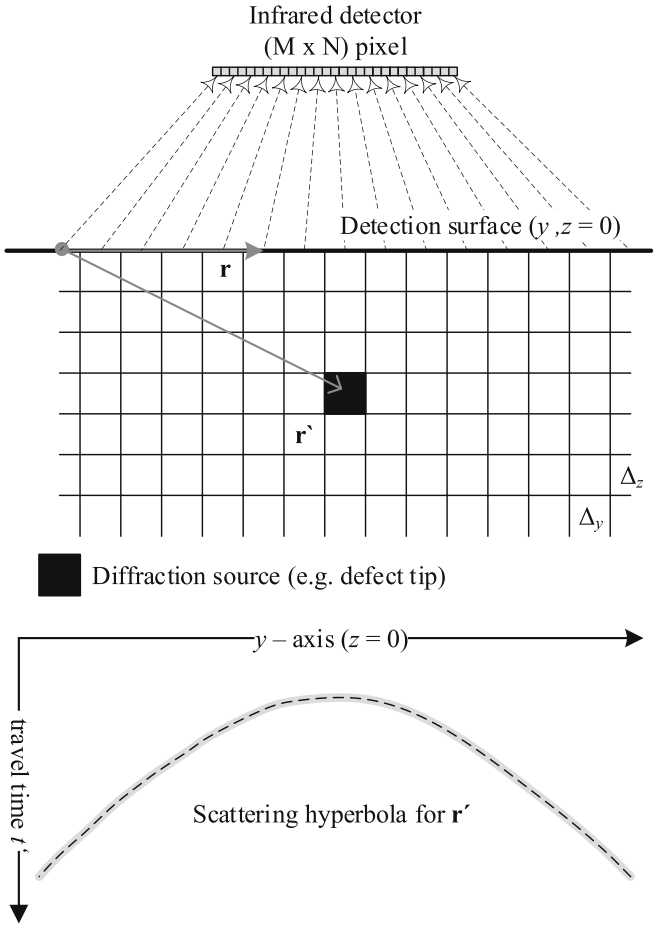

Fig. 2. Principle of T-SAFT.

$$T_0(x',y',z') = \iint_{S_M} T_{\text{virt}}(x,y,0,t')\,\mathrm{d}x\,\mathrm{d}y \qquad (12)$$

$$\text{with} \quad t' = 2\frac{\sqrt{(x-x')^2+(y-y')^2+(z-z')^2}}{c}.$$

In principle T-SAFT is a trial and error method [34]. The assumption is that any defect consists of a number of independent (discrete) point diffraction sources. So, in the first step, the reconstruction space (sample volume) is discretized with $\Delta_y = \Delta_z$. We prescribe any discrete point **r**'. If this point is equal to **r**, the integral of Eq. (12), or in discrete cases, the sum yields a high value. Otherwise the value is low. Performing this operation for each point **r**' gives the final reconstruction image. In this work we apply frequency domain (F)-SAFT. Here, the virtual wave field is transferred into Fourier domain for time and space. The F-SAFT procedure gives the same results as T-SAFT [34], but the F-SAFT method is much faster than T-SAFT [35].

3. Numerical simulation

To test the virtual wave concept with noisy temperature data by respecting prior information, numerical simulation with the FEM are carried out. To do this we consider the 2D model, depicted in Fig. 4 a). The specimen has a length of 100 mm and a height of 10 mm. All boundaries have adiabatic conditions. The slots of the investigated specimen have a width of 3 mm and a height of 0.5 mm with a horizontal distance of $\Delta_y = 10$ mm. The vertical distances with respect to the inspected surface ($z = 0$) are $z_i = (1.75 + i)$ mm ($i = 0, 1, \ldots, 6$). The corresponding defect width-to-depth ratios are sketched in Fig. 4 a). The objective of the FEM simulations is the solution of the direct problem to

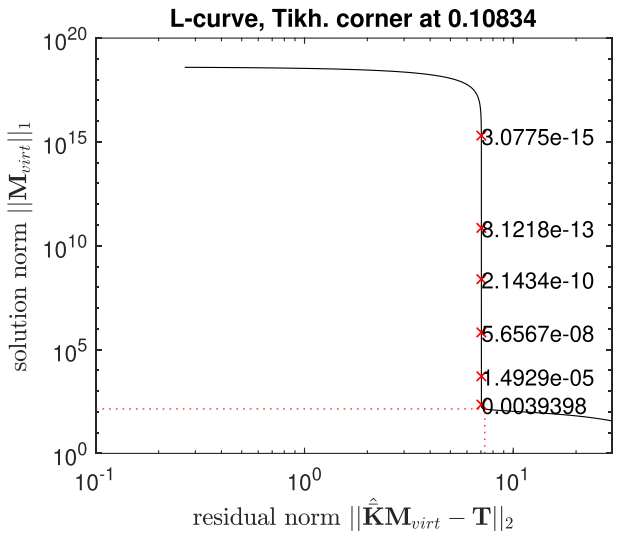

Fig. 3. The regularization parameter λ is found at the edge of the L-Curve. At the edge the best trade off between solution norm and residual norm is located [37]. For the preparation of the L-curve, the Toolbox of [36] was used.

determine the transient temperature field $T(y,z,t)$ in the region of the slots. The initial temperature $T(y,z,t=0)$ is zero. The plane $z = 0$ is heated with an instantaneous and locally uniform pulse. An appropriate simulation time was estimated by $t_{\text{end}} = L^2/\alpha$. The physical parameters are listed in Table 1. Since the virtual speed of sound c can be chosen arbitrarily, we prescribed the dimensionless virtual speed of sound with $\tilde{c} = 1$.

The time resolution Δ_t was 2e-3 s. The temperature data **T** that is depicted in 4 a), was evaluated at $z = 0$ with an equidistant grid and $N_y = 564$ data points. Additionally, the surface temperature was superposed by white Gaussian noise with a standard deviation of $\sigma_0 = 0.0097$ K in order to achieve the same signal to noise ratio SNR $= \max(\mathbf{T})/\sigma_0$ as for the experimental temperature field. Referring to Fig. 1, the **K**-matrix is set up using the physical parameters listed in Table 1 and the corresponding spatial and temporal resolution. This matrix has to be multiplied by the Abel trafo matrix **A** in order to incorporate the additional information positivity. Next, the regularization parameter λ has to be estimated based on the observed temperature data. Therefore, the L-curve method, Fig. 3, is applied. For the preparation of the L-curve the toolbox of [36] was used. For the regularization process applying ADMM, we prescribe the penalty term ρ with 0.0039. Subsequently, the linear severely ill posed problem, namely the calculation of the virtual wave field based on temporal surface temperature data, is solved.

The solution of the inverse problem yields the circular projection $\mathbf{M}_{\text{virt}}$ of the 2D virtual wave field $\mathbf{T}_{\text{virt}}$. Due to this, $\mathbf{M}_{\text{virt}}$ is multiplied by the Abel-trafo matrix **A** to obtain the physically correct 2D virtual wave. The resulting virtual wave field is illustrated in Fig. 4 b). The illustration can be interpreted as superposition of point scatterers. A point scatterer yields a characteristic hyperbola (see Fig. 2), that is rudimentary visible for the first three slots with the highest width-to-depth ratios. In Fig. 5 A-Scans, where virtual waves for different slot positions are represented as a function of depth $z = c{\cdot}t$', are shown. The graphs exhibit a good approximation of the typical 2D wave form.

Referring to Eq. (12), $\mathbf{T}_{\text{virt}}$ is the input for the image reconstruction tool F-SAFT. Since the heat was introduced at $z = 0$, the heat or virtual wave travels to the defect were it is reflected to the surface. Hence, to obtain the correct position of the defect we have to halve the distance or the dimensionless speed of sound $\tilde{c} = 0.5$ for F-SAFT. Fig. 4 d) shows the final image. Let us compare the processed images using the virtual wave concept Fig. 4 c) and the image reconstruction Fig. 4 d). It is visible that F-SAFT improves both sensitivity and the lateral resolution and slots with a defect width-to-depth ratio of 0.52 are detectable. The defect

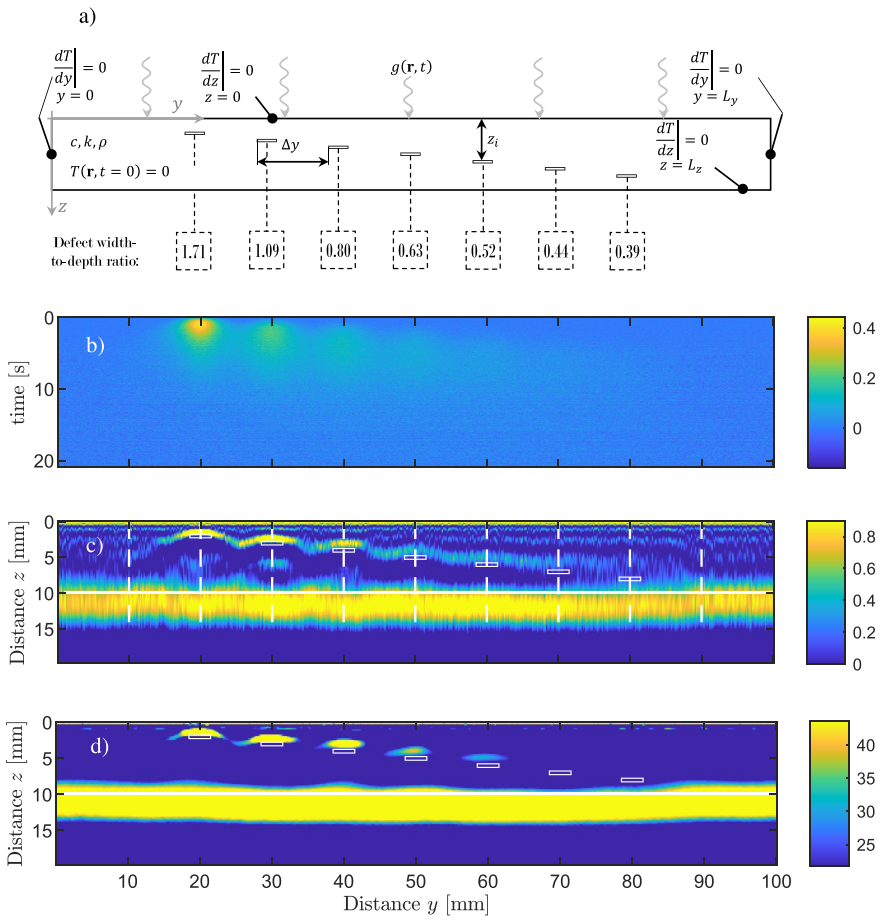

Fig. 4. a) Image reconstruction based on simulated data. Model of the examined specimen with the corresponding boundary conditions. b) Running temperature contrast [1] based on simulated temperature data that is superposed with white Gaussian noise (standard deviation $\sigma = 0.0097$). c) Dimensionless virtual wave field (B-Scan) computed using ADMM and the Abel transformation related to the maximal data point as function of spatial coordinates y, z. d) Reconstructed field computed applying F-SAFT as function of spatial coordinates y, z. The colorbars have the unit Kelvin.

Table 1
Physical parameters for FEM simulation.

Parameter	Value	Unit
thermal conductivity k	15	W m^{-1} K^{-1}
density ρ_M	7800	kg m^{-3}
specific heat capacity c_p	500	J kg^{-1} K^{-1}
thermal diffusivity α	3.85e-06	m^2 s^{-1}

depths were estimated using an A-Scan based on circular projection Fig. 5 a). For the estimation of the defect depths the local maxima after the front-wall echo was evaluated, because these maxima correspond to the reflection at the slot boundaries. The corresponding virtual wave field is shown in Fig. 5 b).

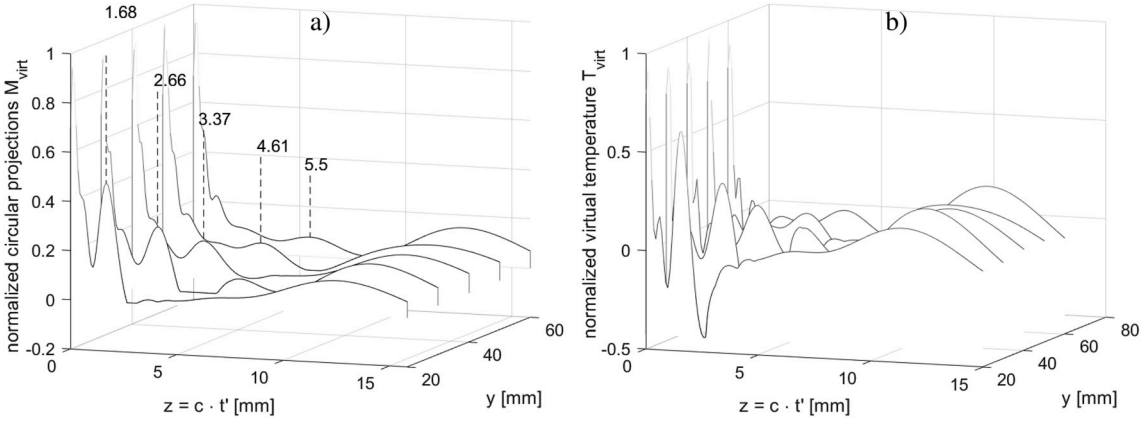

Fig. 5. a) Waterfall plot of the circular projections based on simulated temperature data for different slot positions according to the white dashed line in Fig. 7 b). The numerical markers show the estimated position of the slots. b) Waterfall plot of the Abel transformed circular means or virtual wave field. At $z = 0$ the initial pulse and at $z = L$ the back-wall echo occurs that is denoted by a raise of amplitude. For a defect (slot) an additional virtual wave amplitude occurs at different depths $z = c{\cdot}t'$.

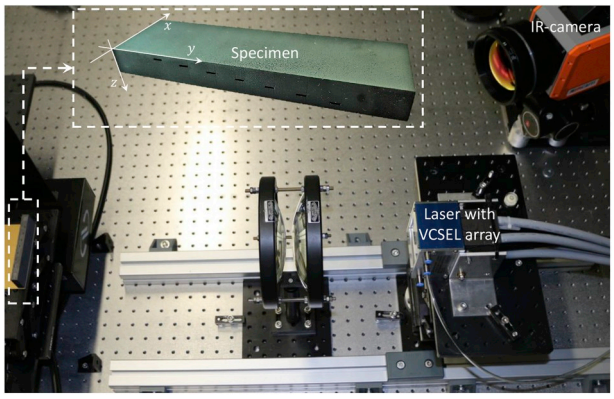

Fig. 6. Metallic specimen (100 mm × 30 mm x 10 mm) with rectangular slots representing defects.

4. Experimental results

4.1. Experimental setup

In order to test the virtual wave concept for pulsed thermography data, we have prepared a metallic specimen with slots representing defects (Fig. 6). The [100 mm × 30 mm x 10 mm] specimen was produced using a cobalt-chromium alloy powder for metal additive manufacturing, also known as metal 3D printing. Additionally, the specimen was coated by diamond-like carbon (DLC). Due to this, the absorption of the flash light radiation and the emissivity is increased. The coating thickness is approximately 7 μm. Therefore, we can assume that the optical material properties of the specimen are homogeneous and isotropic.

In addition to the sample, the experimental setup (see Fig. 6) essentially consists of a laser array for heating and an infrared thermography camera for surface temperature measurement. The laser array is a VCSEL (Vertical-Cavity Surface-Emitting Laser) array with a nominal output power of 2.4 kW [38]. The emitting aperture was imaged onto the sample ($x-y$ plane @ z = 0) using a pair of lenses (distance laser lens approx. 155 mm, distance lens sample approx. 398 mm). The image was slightly defocused to achieve a homogeneous irradiance of 14 $\pm$ 1 W/cm^2 of the entire sample surface, the magnification corresponds to approximately 2.3. The laser was controlled by Labview with pulse lengths of 50 ms. The actual pulse shape was measured using a photodiode and was 50 ms. It was stored frame synchronously in the additional A/D channels of the camera. The temperature-calibrated infrared thermography camera used (InSb-based, 2.5–5.5 μm spectral sensitivity, 100 mm lens, 200 µs integration time) was triggered by the laser pulse with a pretrigger of 1000 frames via the photodiode. In each measurement, 21000 frames were recorded at a frame rate of 1000 Hz, i.e. 1 s before the laser pulse and 20 s after it. The image was taken in full frame mode of 640 × 512 pixels with a spatial resolution of approx. 177 μm per pixel.

4.2. Experimental results

In Fig. 7 a) the measured transient surface temperature is depicted. For the image reconstruction, the mean of 100 surface temperature slices between the pixels 46:145 in x-direction (see Fig. 6) was calculated in order to improve the signal-to-noise ratio. The data set was then temporally downsampled, yielding an evaluation frequency of 500 Hz. The spatial resolution, the physical parameters and the signal to noise ratio SNR = $\max(\mathbf{T})/\sigma_M$, where σ_M is the standard deviation of the measurement data, are equal to the simulated data set (Table 1). The process steps listed in Fig. 1 were then applied again. The corresponding virtual wave field $\mathbf{T}_{\text{virt}}$ is illustrated in Fig. 7 b). Fig. 8 a) illustrates the circular means of the virtual waves for the different slot positions, indicated in Fig. 7 b) by white dashed lines. Fig. 8 b) shows the corresponding virtual waves. At $z = c{\cdot}t' = 0$ the characteristic initial pulse and at $z = L$ the back-wall echo occur. In the center position of the slots $y = \{20, 30, 40, 50, 60\}$ mm an additional peak occurs in the A-Scan. This is because the virtual wave is diffracted at the slot boundaries. The nominal and estimated slot depths using VWC, based on simulated and measurement data, are visible in Fig. 9. The black-dashed line shows the nominal values and is a guide for the eyes. This representation shows, that the slot positions can be detected well, for both simulated and measurement data. For the slot reconstruction based on simulated data,

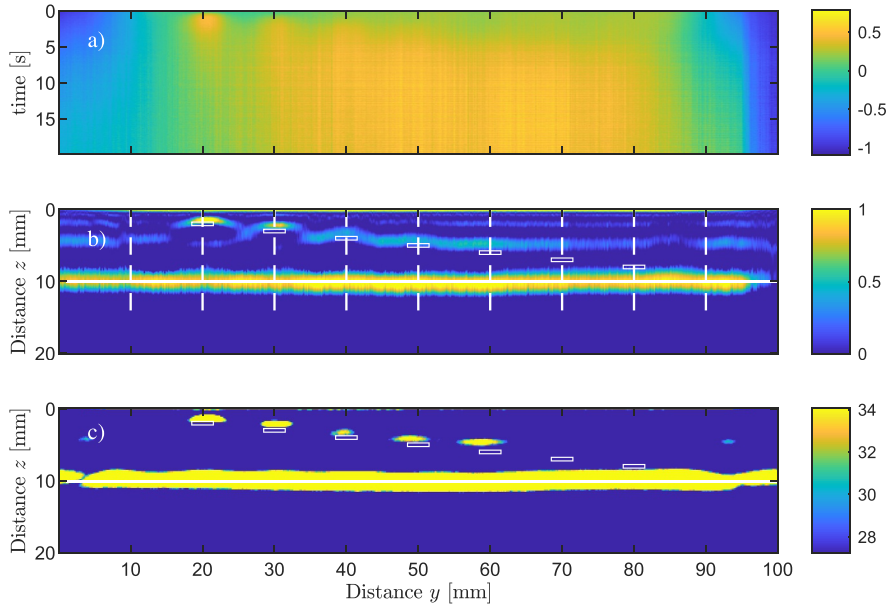

Fig. 7. Image reconstruction based on experimental data. Running temperature contrast based on measured temperature data a), calculated virtual wave field b) using ADMM and reconstructed field applying F-SAFT c). The colorbars have the unit Kelvin.

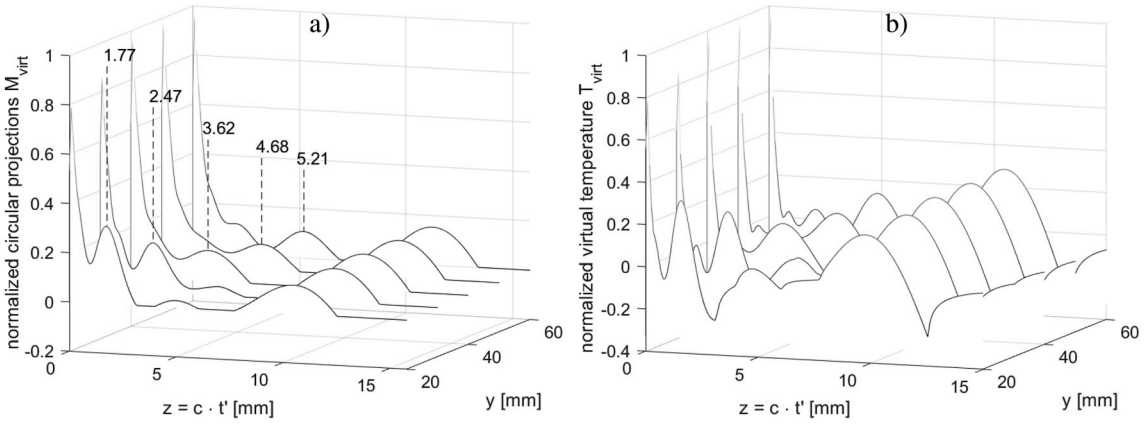

Fig. 8. a) Waterfall plot of the circular projections based on experimental temperature data for different slot positions according to the white dashed line in Fig. 7 b). The numerical markers show the estimated position of the slots. b) Waterfall plot of the Abel transformed circular means or virtual wave field. At $z = 0$ the initial pulse and at $z = L$ the back-wall echo occurs that is denoted by a raise of amplitude. For a defect (slot) an additional virtual wave amplitude occurs at different depths $z = c{\cdot}t'$.

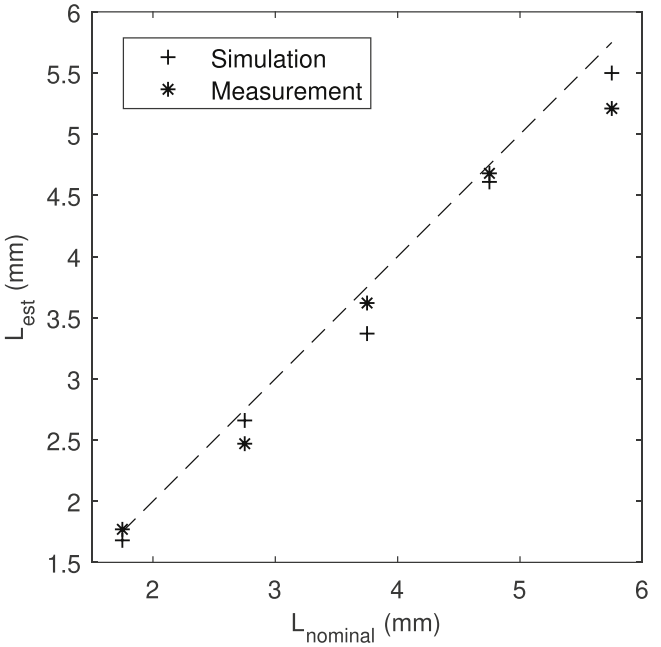

Fig. 9. Nominal positions versus estimated positions for the detectable slots. The black-dashed line indicates the nominal values and is a guide for the eyes. The plus sign exhibits the estimation for simulated data and the asterisk represents the estimated values for the measurement.

we can see a lower intensity of the secondary heat sources for deeper lying defects. The reason for this might result from the growing influence of the back-wall, more precisely from the corresponding boundary. Considering, the simulated data we have adiabatic boundaries, which cause a stronger reflection at the back-wall than for measurement data were the boundaries slightly differ from adiabatic boundaries because of heat convection. Consequently, in contrast to the measurement data, the heat flow in the domain of the deeper lying slots of the simulated data is more affected by the back-wall reflection. We can detect the slots (defects) with a defect width-to-depth ratio of 0.52. Fig. 7 c) depicts the final reconstruction applying F-SAFT to the virtual wave field 7 b). In contrast to the transient virtual wave field the final reconstruction exhibits a much better localization of the slots (defects).

5. Conclusion

In this paper, we have shown an application of the virtual wave concept for 2D pulsed thermography data in reflection mode. Heat diffusion causes entropy production and hence information loss. To compensate the information loss partly, we have incorporated additional information for the regularization process. For the incorporation of positivity as additional information, we have applied the Abel transformation. Here the 2D virtual wave is projected onto a positive data set. Due to this, the inverse problem was reformulated, which yields a new ill-posed inverse problem.

The thermal waves were locally transformed into virtual waves which obey the photoacoustic wave equation. Based on this so called virtual waves, the depth of the slots are detectable by the application of the time of flight method (TOF). Further, we can apply image reconstruction methods from ultrasonic testing. Especially, the F-SAFT algorithm was used for defect reconstruction. The 2D heat diffusion in the region of the slot is respected by the integration along the scattering hyperbolas of the superposed point scatterers. The modified VWC reconstruction based on simulated data was validated with a reconstruction based on experimental data.

Declaration of competing interest

The authors declare that there is no conflict of interest.

CRediT authorship contribution statement

G. Thummerer: Conceptualization, Methodology, Software, Formal analysis, Validation, Investigation, Writing - original draft, Visualization. **G. Mayr:** Conceptualization, Methodology, Writing - original draft, Writing - review & editing, Visualization, Project administration, Funding acquisition. **P.D. Hirsch:** Validation, Investigation, Writing - original draft. **M. Ziegler:** Writing - review & editing. **P. Burgholzer:** Writing - review & editing, Supervision.

Acknowledgement

The financial support by the Austrian Federal Ministry of Science, Research and Economy and the National Foundation for Research, Technology and Development is gratefully acknowledged. Furthermore, this work has been supported by the project “multimodal and in-situ characterization of inhomogeneous materials” (MiCi), by the the federal government of Upper Austria and the European Regional Development Fund (EFRE) in the framework of the EU-program IWB2020.

Gefördert durch die Deutsche Forschungsgemeinschaft (DFG) - 400857558, funded by the Deutsche Forschungsgemeinschaft (DFG, German Research Foundation) - 400857558.

Appendix. 1. Forward problem

The aim of the subsequent steps is to solve the forward problem in two dimensions and free space (without boundaries), based on the 3D virtual *Greens* function $G^{3D}_{\text{virt}}(\mathbf{r},t)$, in order to get a deeper insight how the virtual wave concept works. Therefore, we use the Greens function solution equation (GFSE) for both, diffusion and wave equation [39]. Inserting the respective GFSEs into Eq. (1), yields for the same position vector $\mathbf{r}$ in 3D

$$G^{3D}(\mathbf{r},t) = \int_{-\infty}^{\infty} K(t,t')G^{3D}_{\text{virt}}(\mathbf{r},t')\,\mathrm{d}t' \tag{1}$$

and

$$G^{2D}(\boldsymbol{\rho},t) = \int_{-\infty}^{\infty} K(t,t')G^{2D}_{\text{virt}}(\boldsymbol{\rho},t')\,\mathrm{d}t' \tag{2}$$

in 2D with position vector $\boldsymbol{\rho}$. To calculate $G^{2D}(\boldsymbol{\rho},t)$ we need the 2D virtual Greens function $G^{2D}_{\text{virt}}(\boldsymbol{\rho},t')$. Hence, we start from the 3D virtual Greens function

$$G^{3D}_{\text{virt}}(\mathbf{r},t'|\mathbf{r}',\tau') = \frac{1}{4c\pi}\frac{\partial}{\partial t'}\frac{\delta[c(t'-\tau')-|\mathbf{r}-\mathbf{r}'|)}{|\mathbf{r}-\mathbf{r}'|}. \tag{3}$$

To get the 2D *Greens function* we carry out the integration with respect to z':

$$\begin{aligned} G^{2D}_{\text{virt}}\left(\boldsymbol{\rho},t'|\boldsymbol{\rho}',\tau'\right) &= \int_{-\infty}^{\infty} G^{3D}_{\text{virt}}(\mathbf{r},t'|\mathbf{r}',\tau')\,\mathrm{d}z' \\ &= \frac{1}{4c\pi}\frac{\partial}{\partial t'}\int_{-\infty}^{\infty}\frac{\delta\left[c(t'-\tau')-\sqrt{|\boldsymbol{\rho}-\boldsymbol{\rho}'|^2+z'^2}\right]}{\sqrt{|\boldsymbol{\rho}-\boldsymbol{\rho}'|^2+z'^2}}\,\mathrm{d}z' \end{aligned} \tag{4}$$

with $|\boldsymbol{\rho}-\boldsymbol{\rho}'| = \sqrt{(\mathrm{x}-\mathrm{x}')^2+(\mathrm{y}-\mathrm{y}')^2}$

Now substitute $\mu = \sqrt{|\boldsymbol{\rho}-\boldsymbol{\rho}'|^2+z'^2}$ and use symmetry with respect to the z' axes yields:

$$G^{2D}_{\text{virt}}(\boldsymbol{\rho},t'|\boldsymbol{\rho}',\tau') = \frac{1}{2c\pi}\frac{\partial}{\partial t'}\int_{|\boldsymbol{\rho}-\boldsymbol{\rho}'|}^{\infty}\frac{\delta[c(t'-\tau')-\mu]}{\sqrt{\mu^2-|\boldsymbol{\rho}-\boldsymbol{\rho}'|^2}}\,\mathrm{d}\mu = \frac{1}{2c\pi}\frac{\partial}{\partial t'}\frac{1}{\sqrt{c^2(t'-\tau')^2-|\boldsymbol{\rho}-\boldsymbol{\rho}'|^2}} = \frac{-c^2(t'-\tau')}{2c\pi\left[c^2(t'-\tau')^2-|\boldsymbol{\rho}-\boldsymbol{\rho}'|^2\right]^{3/2}} \quad \text{for} \quad t'>\tau'-\frac{1}{c}|\boldsymbol{\rho}-\boldsymbol{\rho}'|=\gamma. \tag{5}$$

Inserting Eq. (5) into Eq. (2) gives:

$$G^{2D}(\boldsymbol{\rho},t|\boldsymbol{\rho}',\tau') = -\frac{\pi^{-3/2}}{2\sqrt{\alpha t}}\int_{\gamma}^{\infty}\frac{\exp\left(-\frac{c^2(t'-\tau')^2}{4\alpha t}\right)c^2(\tau'-t')\,\mathrm{d}t'}{\left[c^2(t'-\tau')^2-|\boldsymbol{\rho}-\boldsymbol{\rho}'|^2\right]^{3/2}} = -\frac{\exp\left(\frac{-|\boldsymbol{\rho}-\boldsymbol{\rho}'|^2}{4\alpha t}\right)}{2\pi^{3/2}\sqrt{\alpha t}}\int_{\gamma}^{\infty}\frac{\exp\left(\frac{-c^2(t'-\tau')^2+|\boldsymbol{\rho}-\boldsymbol{\rho}'|^2}{4\alpha t}\right)c^2(\tau'-t')\,\mathrm{d}t'}{\left[c^2(t'-\tau')^2-|\boldsymbol{\rho}-\boldsymbol{\rho}'|^2\right]^{3/2}}. \tag{6}$$

Now we substitute $\xi^2 = c^2(t'-\tau')^2-|\boldsymbol{\rho}-\boldsymbol{\rho}'|^2$:

$$G^{2D}(\boldsymbol{\rho},t|\boldsymbol{\rho}',\tau') = -\frac{\exp\left(\frac{-|\boldsymbol{\rho}-\boldsymbol{\rho}'|^2}{4\alpha t}\right)}{2\pi^{3/2}\sqrt{\alpha t}}\int_{0}^{\infty}\frac{\exp\left(\frac{-\xi^2}{4\alpha t}\right)\mathrm{d}\xi}{\xi^2} = -A\int_{0}^{\infty}\frac{\exp\left(\frac{-\xi^2}{4\alpha t}\right)\mathrm{d}\xi}{\xi^2}. \tag{7}$$

Integration by parts yields:

$$\frac{G^{2D}(\boldsymbol{\rho},t|\boldsymbol{\rho}',\tau')}{A} = 2\int_{0}^{\infty}\frac{\exp\left(\frac{-\xi^2}{4\alpha t}\right)}{4\alpha t}\,\mathrm{d}\xi = \sqrt{4\pi\alpha t}\,\mathrm{erf}\left(\frac{\xi^2}{\sqrt{4\alpha t}}\right)|_0^{\infty} = \frac{\sqrt{\pi}}{\sqrt{4\alpha t}} \tag{8}$$

Replacing A in Eq. (8) gives:

$$G^{2D}(\boldsymbol{\rho},t|\boldsymbol{\rho}',\tau') = A\frac{\sqrt{\pi}}{\sqrt{4\alpha t}} = \frac{\exp\left(\frac{-|\boldsymbol{\rho}-\boldsymbol{\rho}'|^2}{4\alpha t}\right)}{2\pi^{3/2}\sqrt{\alpha t}}\frac{\sqrt{\pi}}{\sqrt{4\alpha t}} = \frac{1}{4\pi\alpha t}\exp\left(\frac{-|\boldsymbol{\rho}-\boldsymbol{\rho}'|^2}{4\alpha t}\right) \tag{9}$$

This is exactly the *Greens function* for a 2D body with infinite extension [40]. We note, that the Greens function for heat conduction in 2D and free space is deductible by VWC. Applying the method of images, Eq. (9) is readily extended for Dirichlet and Neumann boundaries or a mix of them [41].

References

[1] Maldague XPV. Theory and practice of infrared technology for nondestructive testing. New York and Chichester: A Wiley-Interscience publication, Wiley; 2001.

[2] Vavilov VP, Burleigh DD. Review of pulsed thermal ndt: physical principles, theory and data processing. NDT E Int 2015;73:28–52. https://doi.org/10.1016/j.ndteint.2015.03.003.

[3] Burgholzer P. Thermodynamic limits of spatial resolution in active thermography. Int J Thermophys 2015;36(9):2328–41. https://doi.org/10.1007/s10765-015-1890-7.

[4] Almond DP, Pickering SG. An analytical study of the pulsed thermography defect detection limit. J Appl Phys 2012;111(9):093510. https://doi.org/10.1063/1.4704684.

[5] Oswald-Tranta B. Time and frequency behaviour in tsr and ppt evaluation for flash thermography. Quant InfraRed Thermogr J 2017;14(2):164–84. https://doi.org/10.1080/17686733.2017.1283743.

[6] Ranjit S, Choi M, Kim W. Quantification of defects depth in glass fiber reinforced plastic plate by infrared lock-in thermography. J Mech Sci Technol 2016;30(3):1111–8. https://doi.org/10.1007/s12206-016-0215-5.

[7] Liu JY, Gong JL, Qin L, Guo B, Wang Y. Three-dimensional visualization of subsurface defect using lock-in thermography. Int J Thermophys 2015;36(5–6):1226–35. https://doi.org/10.1007/s10765-014-1717-y.

[8] Kaiplavil S, Mandelis A. Truncated-correlation photothermal coherence tomography for deep subsurface analysis. Nat Photon 2014;8(8):635–42. https://doi.org/10.1038/NPHOTON.2014.111.

[9] Tavakolian P, Sivagurunathan K, Mandelis A. Enhanced truncated-correlation photothermal coherence tomography with application to deep subsurface defect imaging and 3-dimensional reconstructions. J Appl Phys 2017;122(2):023103. https://doi.org/10.1063/1.4992807.

[10] Orlande HRB. Thermal measurements and inverse techniques, Heat transfer. Boca Raton, FL: CRC Press; 2011.

[11] Richter R, Maierhofer C, Kreutzbruck M. Numerical method of active thermography for the reconstruction of back wall geometry. NDT E Int 2013;54:189–97. https://doi.org/10.1016/j.ndteint.2012.10.010.

[12] Dizeu FBD, Laurendeau D, Bendada A. Non-destructive testing of objects of complex shape using infrared thermography: rear surface reconstruction by temporal tracking of the thermal front. Inverse Probl 2016;32(12):125007. https://doi.org/10.1088/0266-5611/32/12/125007.

[13] Pawar SS, Vavilov VP. Applying the heat conduction-based 3d normalization and thermal tomography to pulsed infrared thermography for defect characterization in composite materials. Int J Heat Mass Tran 2016;94:56–65. https://doi.org/10.1016/j.ijheatmasstransfer.2015.11.018.

[14] Mendioroz A, Martínez K, Celorrio R, Salazar A. Characterizing the shape and heat production of open vertical cracks in burst vibrothermography experiments. NDT E Int 2019;102:234–43. https://doi.org/10.1016/j.ndteint.2018.12.006.

[15] Holland SD, Schiefelbein B. Model-based inversion for pulse thermography. Exp Mech 2019;59(4):413–26. https://doi.org/10.1007/s11340-018-00463-2.

[16] Burgholzer P, Thor M, Gruber J, Mayr G. Three-dimensional thermographic imaging using a virtual wave concept. J Appl Phys 2017;121(10):105102. https://doi.org/10.1063/1.4978010.

[17] Lee KH, Liu G, Morrison HF. A new approach to modeling the electromagnetic response of conductive media. Geophysics 1989;54(9):1180–92. https://doi.org/10.1190/1.1442753.

[18] Lee KH, Xie G. A new approach to imaging with low–frequency electromagnetic fields. Geophysics 1993;58(6):780–96. https://doi.org/10.1190/1.1443464.

[19] Gershenson M. Simple interpretation of time–domain electromagnetic sounding using similarities between wave and diffusion propagation. Geophysics 1997;62(3):763–74. https://doi.org/10.1190/1.1444186.

[20] Hansen PC. Rank-deficient and discrete ill-posed problems: numerical aspects of linear inversion/Per Christian Hansen, SIAM monographs on mathematical modeling and computation. Philadelphia, Pa.: SIAM; 1998.

[21] Aster RC, Borchers B, Thurber CH. Parameter estimation and inverse problems. third ed. Edition. Amsterdam: Elsevier; 2018.

[22] Burgholzer P, Bauer-Marschallinger J, Grün H, Haltmeier M, Paltauf G. Temporal back-projection algorithms for photoacoustic tomography with integrating line detectors. Inverse Probl 2007;23(6):S65–80. https://doi.org/10.1088/0266-5611/23/6/S06.

[23] Finch D, Haltmeier M, Rakesh. Inversion of spherical means and the wave equation in even dimensions. SIAM J Appl Math 2007;68(2):392–412. https://doi.org/10.1137/070682137.

[24] Mayr G, Stockner G, Plasser H, Hendorfer G, Burgholzer P. Parameter estimation from pulsed thermography data using the virtual wave concept. NDT E Int 2018;100:101–7. https://doi.org/10.1016/j.ndteint.2018.09.003.

[25] Almond D, Patel P. Photothermal science and techniques, Vol. 10 of Physics and its applications. London: Chapman & Hall; 1996.

[26] Wang LV. Photoacoustic imaging and spectroscopy, Vol. 144 of Optical science and engineering. Boca Raton: CRC Press; 2009.

[27] Paltauf G, Nuster R, Passler K, Haltmeier M, Burgholzer P. Optimizing image resolution in three-dimensional photoacoustic tomography with line detectors. In: SPIE proceedings. SPIE; 2008. p. 685621. https://doi.org/10.1117/12.763161.

[28] Paltauf G, Nuster R, Haltmeier M, Burgholzer P. Experimental evaluation of reconstruction algorithms for limited view photoacoustic tomography with line detectors. Inverse Probl 2007;23(6):S81–94. https://doi.org/10.1088/0266-5611/23/6/S07.

[29] Boyd S. Distributed optimization and statistical learning via the alternating direction method of multipliers. Found Trends® Mach Learn 2010;3(1):1–122. https://doi.org/10.1561/2200000016.

[30] Parikh N. Proximal algorithms. Found Trends® Optim 2014;1(3):127–239. https://doi.org/10.1561/2400000003.

[31] Hansen PC. The L-curve and its use in the numerical treatment of inverse problems. IMM-REP, IMM, Department of Mathematical Modelling, Technical University of Denmark; 1999. D. T. U. I. f. M. Modellering, T. U. o. D. D. o. M. Modelling, DTU, https://books.google.at/books?id=Ge-cXwAACAAJ.

[32] Mayer K, Marklein R, Langenberg KJ, Kreutter T. Three-dimensional imaging system based on fourier transform synthetic aperture focusing technique. Ultrasonics 1990;28(4):241–55. https://doi.org/10.1016/0041-624X(90)90091-2.

[33] Busse LJ. Three-dimensional imaging using a frequency-domain synthetic aperture focusing technique. IEEE Trans Ultrason Ferroelectrics Freq Contr 1992;39(2):174–9. https://doi.org/10.1109/58.139112.

[34] Langenberg K-J, Marklein R, Mayer K. Ultrasonic nondestructive testing of materials: theoretical foundations/Karl-Jorg Langenberg, Rene Marklein, Klaus Mayer. Boca Raton: Taylor & Francis; 2012.

[35] Marklein R, Mayer K, Hannemann R, Krylow T, Balasubramanian K, Langenberg KJ, Schmitz V. Linear and nonlinear inversion algorithms applied in nondestructive evaluation. Inverse Probl 2002;18(6):1733–59. https://doi.org/10.1088/0266-5611/18/6/319.

[36] Hansen PC. Regularization tools version 4.0 for matlab 7.3. Numer Algorithm 2007;46(2):189–94. https://doi.org/10.1007/s11075-007-9136-9.

[37] Hansen PC. Discrete inverse problems: insight and algorithms, Fundamentals of algorithms. Philadelphia: Society for Industrial and Applied Mathematics; 2010.

[38] Ziegler M, Thiel E, Studemund T. Thermography using a 1d laser array – from planar to structured heating. Mater Test 2018;60(7–8):749–57. https://doi.org/10.3139/120.111209.

[39] Hahn DW. Heat conduction. third ed. Hoboken N.J.: Wiley; 2012.

[40] Cole KD. Heat conduction using Green's functions, 2nd Edition, Series in computational and physical processes in mechanics and thermal sciences. Boca Raton: CRC Press; 2011.

[41] Morse PM, Feshbach H. Methods of theoretical physics, International series in pure and applied physics. Boston Mass.: McGraw-Hill; 1953.